Dramatic changes in Harbin aerosol during 2018–2020: the roles of open burning policy and secondary aerosol formation

Yuan Cheng[1], Qin-qin Yu[1], Jiu-meng Liu[1,*], Xu-bing Cao[1], Ying-jie Zhong[1], Zhen-yu Du[2], Lin-lin Liang[3], Guan-nan Geng[4], Wan-li Ma[1], Hong Qi[1], Qiang Zhang[5], Ke-bin He[4]

[1] State Key Laboratory of Urban Water Resource and Environment, School of Environment, Harbin Institute of Technology, Harbin, China

[2] National Research Center for Environmental Analysis and Measurement, Environmental Development Center of the Ministry of Ecology and Environment, Beijing, China

[3] State Key Laboratory of Severe Weather & CMA Key Laboratory of Atmospheric Chemistry, Chinese Academy of Meteorological Sciences, Beijing, China

[4] State Key Joint Laboratory of Environment Simulation and Pollution Control, School of Environment, Tsinghua University, Beijing, China

[5] Department of Earth System Science, Tsinghua University, Beijing, China

[*] Corresponding author. Jiu-meng Liu (jiumengliu@hit.edu.cn).

Abstract

Despite the growing interest in understanding haze formation in Chinese megacities, air pollution has been largely overlooked for the Harbin-Changchun (HC) metropolitan area located in the severe cold climate region in Northeast China. In this study, we unfolded significant variations of fine particulate matter ($PM_{2.5}$) in HC's central city (Harbin) during two sequential heating seasons of 2018–2019 and 2019–2020, and explored major drivers for the observed variations. The two campaigns showed comparable organic carbon (OC) levels but quite different OC sources. The biomass burning (BB) to OC contribution decreased substantially for 2019–2020, which was attributed primarily to the transition of local policies on agricultural fires, i.e., from the "legitimate burning" policy released in 2018 to the "strict prohibition" policy in 2019. Meanwhile, the contribution of secondary OC (OC_{sec}) increased significantly, associated with the much more frequent occurrences of high relative humidity (RH) conditions during the 2019–2020 measurement

period. Similar to OC_{sec}, the major secondary inorganic ions, i.e., sulfate, nitrate and ammonium (SNA), also exhibited RH-dependent increases. Given the considerable aerosol water contents predicted for the high-RH conditions, heterogeneous reactions were likely at play in secondary aerosol formation even in the frigid atmosphere in Harbin (e.g., with daily average temperatures down to below –20 °C). In brief, compared to 2018–2019, the 2019–2020 measurement period was characterized by a policy-driven decrease of biomass burning OC, a RH-related increase of OC_{sec} and a RH-related increase of SNA, with the former two factors generally offsetting each other. In addition, we found that open burning activities were actually not eliminated by the "strict prohibition" policy released in 2019, based on a synthesis of air quality data and fire count results. Although not occurred during the 2019–2020 measurement period, agricultural fires broke out within a short period before crop planting in spring of 2020, and resulted in off-the-chart air pollution for Harbin, with 1- and 24-hour $PM_{2.5}$ concentrations peaking at ~2350 and 900 μg/m^3, respectively. This study indicates that sustainable use of crop residues remains a difficult challenge for the massive agricultural sector in Northeast China.

1. Introduction

Despite nationwide reductions in anthropogenic emissions (Zhang et al., 2019), severe haze pollution characterized by high concentrations of fine particulate matter ($PM_{2.5}$) is far from being effectively controlled in China, e.g., haze episodes were observed in Beijing even during the COVID-19 lockdown (Lv et al., 2020). This reveals the complex yet poorly understood responses of air pollution to changes of primary emission. While secondary aerosol production has been thought to be largely responsible for this lack of understanding, the chemical mechanisms remain vague (Le et al., 2020; Wang et al., 2020b; Huang et al., 2021). For example, state-of-the-art models incorporating gas-phase and cloud chemistry frequently underestimated sulfate and secondary organic aerosol (SOA) concentrations for winter haze events in Beijing (Wang et al., 2014; Zheng et al., 2015a; Cheng et al., 2016; Liu et al., 2020a). The underestimation was more significant with increasing relative humidity (RH) or aerosol water content (AWC) levels, pointing to the importance of aqueous-phase reactions in aerosol water (Wang et al., 2016; Shrivastava et al., 2017; Su et al., 2020; Liu et al., 2021b). On the other hand, quantitative prediction of secondary aerosols formed through aqueous-phase reactions remains challenging, partially due to uncertainties in aerosol pH (Guo et al., 2017b; Song et al., 2018; Zheng et al., 2020) and oxidant concentrations (Ye et al., 2018; Wang et al., 2020a). In addition, despite the role of heterogeneous chemistry has been widely accepted for sulfate formation, its effects on SOA remain unclear, with more evidences indicating an enhancement effect (Hu et al., 2016; Kuang et al., 2020; Liu et al., 2020a; Wang et al., 2021a) overwhelming those suggesting little influence of RH or AWC on SOA formation (Zheng et al., 2015b). In all, there is a growing interest in understanding haze pollution in Chinese megacities (Shi et al., 2019), especially regarding the driving factors responsible for the spatio-temporal variations,

since these factors are essential for the development of efficient air pollution control strategies.

Studies on haze in China have been historically concentrated in the North China Plain (NCP), especially around Beijing. Recently, new hotspots began to emerge, e.g., the Harbin-Changchun (HC) metropolitan area. HC is located in the severe cold climate region in Northeast China, and includes 11 cities in the two provinces of Heilongjiang and Jilin. Compared to NCP and other traditional hotspots of air pollution research (e.g., the Yangtze River Delta), HC is characterized by its extremely cold winter when the daily average temperatures could drop to below –20 °C. Thus, the heating season is usually as long as six months in HC, lasting from late fall through early spring of next year. During this period, intensive energy use is expected, e.g., coal combustion for central heating in urban areas and household biomass burning for space-heating in rural areas. The intensive energy use, to a large extent, determines the relatively high baseline of $PM_{2.5}$ pollution in HC's heating season. According to the open access air quality data routinely published by China National Environmental Monitoring Center (http://106.37.208.233:20035/), the monthly averages of $PM_{2.5}$ measured during winter in Harbin stayed above 55 $\mu g/m^3$ from 2013 throughout 2020, whereas the corresponding value could drop to below 30 $\mu g/m^3$ for Beijing.

Another feature of HC is that it is located in a main agricultural region in China. For example, Heilongjiang Province provided ~13% and 15% of the national rice and corn productions in 2019, respectively, with only ~5% of China's land area (National Bureau of Statistics of China, 2020). The massive agricultural sector results in a huge amount of crop residues, which are produced after harvesting in autumn and must be disposed before planting in spring of the next year. Although nominally prohibited, open burning persists as an important approach for the disposal of crop residues in Northeast China, with a time window largely overlapped with the heating season. These

agricultural fires frequently resulted in heavily-polluted $PM_{2.5}$ episodes, e.g., with 24-hour $PM_{2.5}$ peaking at ~650 μg/m^3 during early November of 2015 in Harbin (Li et al., 2019b). Given that the agricultural fires were never eliminated, interim provisions were released by Heilongjiang Province in 2018, which approved a window of approximately 3 months (from 11 December, 2018 to 9 March, 2019) for open burning of crop residues (Department of Ecology and Environment of Heilongjiang Province, 2018). However, the interim provisions were amended in 2019, i.e., the "legitimate burning" policy was terminated and was replaced by a toughest-ever policy on open burning, which required that agricultural fires should be strictly prohibited for the period of 15 September, 2019 to 15 May, 2020. The rapid transition of open burning policy reflects the ongoing attempts of local government to control the severe haze pollution caused by agricultural fires. However, the most effective and reliable approach remains inconclusive, given that very little is known about the role of biomass burning in $PM_{2.5}$ pollution in Northeast China. Actually, $PM_{2.5}$ in Northeast China is far from being well characterized yet with limited studies (e.g., Cao et al., 2016; Yang et al., 2017; Li et al., 2019b; Zhang et al., 2020), especially regarding sources and chemical mechanisms of aerosol formation.

In this study, we investigated the variations of Harbin aerosol during two sequential heating seasons of 2018–2019 and 2019–2020, with focuses on the roles of (1) rapid transition of open burning policy and (2) significant change of meteorological conditions (especially relative humidity), which would influence primary emissions and secondary aerosol formation, respectively. Policy implications for improving air quality in the HC region were also discussed.

2. Methods

2.1 Field observation and additional data sets used

Two campaigns were conducted at an urban site located in the campus of Harbin Institute of Technology (HIT; 45°45′24″ N, 126°40′49″ E) during the heating seasons of 2018–2019 (from 16 October, 2018 to 14 April, 2019; N = 180) and 2019–2020 (from 16 October, 2019 to 4 February, 2020; N = 112), following the same sampling and analytical procedures. As described for the 2018–2019 campaign (Cheng et al., 2021a), a low volume sampler (MiniVol; Airmetrics, OR, USA) operated at a flow rate of 5 L/min was used to collect airborne $PM_{2.5}$ onto pre-baked quartz-fiber filters (2500 QAT-UP; Pall Corporation, NY, USA), and the measured species included organic carbon (OC), elemental carbon (EC), organic tracers for biomass burning (levoglucosan and mannosan) and water-soluble inorganic ions (sulfate, nitrate, ammonium, etc.). Briefly, OC and EC were determined by a thermal/optical carbon analyzer (DRI-2001; Atmoslytic Inc., CA, USA), using the IMPROVE-A temperature protocol with transmittance charring correction. Precision of the carbon analyzer was investigated by analyzing the samples using another protocol (NIOSH). Comparisons of total carbon and optical attenuation results between the two protocols suggested good repeatability for both the carbon and transmittance measurements (Figure S1). Levoglucosan and mannosan were detected by a Dionex ion chromatography (IC) system (ICS-5000$^+$; Thermo Fisher Scientific Inc., MA, USA), using the high-performance anion-exchange chromatography coupled to pulsed amperometric detection (HPAEC-PAD) method. In addition, the IC was also used to measure the inorganic ions. Precision of the IC was evaluated by analyzing selected solutions 5–10 times, and the relative standard deviations were found to be within 5% for all the water-soluble species detected, either organic or inorganic. Based on the observed aerosol components, $PM_{2.5}$ mass was reconstructed as the sum of organic matter (determined as 1.6 × OC), EC and inorganic ions. The reconstructed $PM_{2.5}$ will be specified as $(PM_{2.5})^*$ in the flowing discussions.

Air quality data including $PM_{2.5}$, sulfur dioxide (SO_2), nitrogen dioxide (NO_2), carbon monoxide (CO), etc. were obtained from China's National Urban Air Quality Real Time Publishing Platform (http://106.37.208.233:20035/). They were measured at monitoring sites operated by the China National Environmental Monitoring Center (CNEMC), and could be accessed with a time resolution of 1 hour. There are a total of 12 CNEMC sites in Harbin. Results from the nearest one to the filter sampling site (~2.4 km apart), i.e., Taiping Hongwei Park, were used in this study. In addition, hourly meteorological data including temperature and relative humidity (RH) were obtained from Weather Underground (https://www.wunderground.com).

Using levoglucosan as the reference component, the relative abundances of water-soluble potassium (K^+) were found to increase substantially for five samples collected during the Chinese New Year periods in February of 2019 ($N = 2$; Cheng et al., 2021a) and in January of 2020 ($N = 3$; Figure S2), pointing to significant influence of firework emissions. Given that such emissions may result in primary sulfate and nitrate which are difficult to quantify, the firework events were excluded, and the remaining sulfate and nitrate were considered secondary in the following discussions. Then taking together observational results from the filter sampling and CNEMC sites, the sulfur oxidation ratio (SOR) was determined as the molar ratio of sulfate to the sum of sulfate and SO_2, and the nitrogen oxidation ratio (NOR) was determined similarly based on nitrate and NO_2.

2.2 Thermodynamic simulation

The ISORROPIA-II model (Fountoukis and Nenes, 2007) was used to predict aerosol water content (AWC) and aerosol pH. The calculations were conducted in two ways, namely the “reverse” and “forward” modes. For the “reverse” mode, the measured aerosol-phase data were deployed as input to derive AWC and pH directly. For the “forward” mode, the model was run in an iteration

151 way (Liu et al., 2021a). Briefly, we used the measured aerosol-phase data as initial input, ran
152 ISORROPIA-II in the "forward" mode to predict gas-phase concentrations of semi-volatile species
153 (e.g., ammonia and nitric acid), and used the sum of predicted gas-phase and measured aerosol-
154 phase concentrations as the input for next round. The calculations were repeated until the simulated
155 results were stable and in line with the observational data. Although the "reverse" and "forward"
156 mode simulations showed comparable AWC levels for this campaign (Figure S3), the latter
157 approach has been suggested to give more accurate and robust estimation of pH (Guo et al., 2017a;
158 Song et al., 2018). Thus, AWC and pH results predicted by the iteration approach were used in the
159 following discussions.

160 **2.3 Source apportionment**

161 Source apportionment was performed using EPA's Positive Matrix Factorization (PMF) model
162 (version 5.0), with times series of OC, EC, levoglucosan, chloride, nitrate, sulfate and ammonium
163 from both campaigns as inputs. A total of five factors were resolved, and their profiles were shown
164 in Figure S4. Two factors (BB-1 and BB-2) were strongly associated with primary biomass burning
165 emissions, since almost all the levoglucosan (~90%) were apportioned to these two factors whereas
166 neither of them was a major contributor to secondary ions. Another two factors were inferred to
167 represent secondary aerosols (SA-1 and SA-2), as they had zero EC but the majority of nitrate and
168 sulfate. The last factor (non-BB_{pri}) was attributed to primary emissions from non-BB sources,
169 because more than 50% of EC but little levoglucosan was found in this factor.

170 **3. Results and discussion**

171 **3.1 Variation of biomass burning (BB) OC**

172 Although comparable OC levels were observed during the 2018–2019 and 2019–2020

measurement periods (averaging 20.66 ± 18.17 and 20.64 ± 16.76 μgC/m^3, respectively), the former campaign exhibited substantially higher contributions of levoglucosan to OC (Figure 1a). Here we applied the levoglucosan to OC ratio (LG/OC) as the indicator for BB impact, given that the absolute concentrations of ambient levoglucosan could be influenced by other factors in addition to biomass burning (e.g., wind speed and planetary boundary layer height). LG/OC averaged 1.83 ± 1.18 and 1.17 ± 0.30% (on a basis of carbon mass) during 2018–2019 and 2019–2020, respectively, indicating that the influence of biomass burning was stronger during the former campaign. This difference was mainly caused by the 2018–2019 samples collected during and after the "legitimate burning" periods (periods of P-2 and P-3, with average LG/OC ratios of 2.09 ± 1.42 and 2.15 ± 0.94%, respectively; Figure 1b), whereas the LG/OC ratios observed before the onset of "legitimate burning" (P-1, averaging 1.20 ± 0.36%) were in general comparable with those during the 2019–2020 campaign.

Recalling the different open burning policies released in 2018 and 2019, the observed variations of LG/OC appeared to be associated with agricultural fires. According to the relationship between levoglucosan and OC, Cheng et al. (2021a) classified the 2018–2019 samples into three groups (Cases A, B and C) with LG/OC ranges of < 1.5%, 1.5–3.0% and > 3.0%, respectively. Levoglucosan exhibited strong linear correlations with OC for all the three cases ($r \geq 0.95$), with slopes, i.e., ΔLG/ΔOC (approximately equivalent to LG/OC given the close-to-zero intercepts), of 1.1, 2.3 and 5.0%, respectively. The variation of LG/OC across the three cases was inferred to be driven mainly by agricultural fires that had relatively low combustion efficiencies, based on a synthesis of the following evidences (Cheng et al., 2021a): (1) the levoglucosan to K^+ ratios and levoglucosan to mannosan ratios observed throughout the 2018–2019 campaign were in line with the characteristics of BB smoke emitted by the burning of crop residues; (2) no dependence of

LG/OC on temperature was observed, indicating that the variations of LG/OC could not be explained by biomass burning for household space-heating in rural areas; (3) elevated LG/OC ratios were typically associated with intensive fire counts, i.e., open burning of crop residues, around Harbin; (4) chemical signatures associated with combustion phase exhibited changes toward smoldering-dominated burning from Cases A through C, e.g., ΔEC/ΔCO (derived from linear regression of EC on CO) decreased whereas the levoglucosan to K^+ ratios increased. Following Cheng et al. (2021a), LG/OC ratios higher than 1.5% were considered an indicator for apparent impacts of agricultural fires around Harbin. As shown in Figures 1c–1d, approximately 50% of the 2018–2019 samples exhibited LG/OC above 1.5%, with various fractions for the three periods, i.e., 15, 64 and 71% for P-1, P-2 and P-3 samples, respectively. Thus, apparent impacts of agricultural fires were frequently encountered in the 2018–2019 campaign, particularly after the onset of "legitimate burning". It is noteworthy that the agricultural fires did not actually disappear after the ending of "legitimate burning" and instead extended to mid-April of 2019. For the 2019–2020 campaign, however, only less than 5% of the samples showed LG/OC larger than 1.5% (Figure 1c), indicating the rare occurrence of agricultural fires during the measurement period.

Comparison of source apportionment results between the two campaigns also indicated substantial changes in the influence of agricultural fires. For the 2018–2019 campaign, both the OC mass apportioned to BB-1 ($OC_{BB\text{-}1}$; Figure S5) and the contribution of BB-1 to OC ($f_{BB\text{-}1}$; Figure 2) increased substantially after the onset of "legitimate burning", likely indicating that this factor was representative of agricultural fire emissions. This inference was also supported by the comparison of OC source apportionment results across the three cases (A–C) with increasing LG/OC ratios, i.e., with stronger impacts of agricultural fires. $OC_{BB\text{-}1}$ increased drastically by ~25 folds (from 1.2 to

217 30.9 μgC/m^3) from Cases A through C, with OC attributed to other factors being largely unchanged,
218 and correspondingly, $f_{BB\text{-}1}$ increased sharply from 9 to 69% across the three cases (Figure S6). In
219 addition, it was noticed that negligible EC was apportioned to the BB-1 factor (Figure S4), which
220 was the characteristic of smoldering-dominated combustion as supported by numerous BB source
221 emission studies (McMeeking et al., 2009; May et al., 2014; Pokhrel et al., 2016; McClure et al.,
222 2020; Wang et al., 2020c). This feature was consistent with the inference that the agricultural fires
223 had relatively low combustion efficiencies (Cheng et al., 2021a). During the 2018–2019 campaign,
224 the contribution of agricultural fires to OC was rather small (9%) before the onset of "legitimate
225 burning", whereas after this time point, the contribution increased to ~40% (Figure 2). The overall
226 $f_{BB\text{-}1}$ was 34% for the entire measurement period of 2018–2019, suggesting agricultural fire
227 emissions as the dominant source of OC. For the 2019–2020 campaign, however, $f_{BB\text{-}1}$ was
228 substantially lower (9%; Figure 2), comparable with that determined for the 2018–2019 samples
229 collected during P-1, i.e., before the onset of "legitimate burning". Regarding the temporal variation
230 of agricultural fire impacts, therefore, the same patterns were observed based on the comparisons of
231 LG/OC and PMF results across various measurement periods.

232 Unlike $OC_{BB\text{-}1}$, OC masses apportioned to the BB-2 factor ($OC_{BB\text{-}2}$) were comparable for the
233 2018–2019 samples collected before, during and after the "legitimate burning" periods (Figure S5).
234 $OC_{BB\text{-}2}$ was also largely unchanged across the three cases (A–C) with stronger impacts of
235 agricultural fires (Figure S6). Therefore, it seems that BB-2 was associated with biomass burning
236 activities that did not have significant daily variation, with the most likely candidate being
237 household combustion of crop residues (for cooking and heating). In addition, $OC_{BB\text{-}2}$ appeared to
238 be slightly higher for the 2019–2020 campaign compared to 2018–2019 (6.24 vs. 4.51 μgC/m^3;

239 Figure S5), presumably because more crop residues were consumed through household use in
240 response to the "strict prohibition" open burning policy.

241 The two biomass burning factors constituted 57% of OC for the 2018–2019 campaign (Figure
242 2). Before the onset of "legitimate burning", the total contribution of biomass burning (f_{BB}) was 46%
243 and was dominated by the BB-2 factor (i.e., household burning of crop residues), whereas after this
244 time point, f_{BB} increased to 59% and was dominated by BB-1 (agricultural fires). For the Case C
245 samples, i.e., under the strongest impacts of agricultural fires, f_{BB} was as high as 79% (Figure S6).
246 A prominent reduction in $OC_{BB\text{-}1}$, however, occurred for the 2019–2020 measurement period, and
247 f_{BB} dropped to 39% with BB-2 as the dominant contributor (Figures 2 and S5). It is noteworthy that
248 compared to the typical f_{BB} determined during winter in Beijing (~10–20%, derived from field
249 observations using aerosol mass spectrometer; Hu et al., 2016; Sun et al., 2018; Li et al., 2019a; Xu
250 et al., 2019), the BB contributions were much higher in Harbin even when the contribution of
251 agricultural fires was limited (e.g., during the 2019–2020 campaign, and P-1 in 2018–2019),
252 pointing to strong emissions from residential burning of crop residues throughout the heating season
253 in Northeast China.

254 **3.2 Variation of secondary OC**

255 OC masses apportioned to the SA-1 and SA-2 factors (OC_{sec}) were considered secondary. OC_{sec}
256 were 3.9 and 7.6 μgC/m^3 for the 2018–2019 and 2019–2020 campaigns, respectively, constituting
257 19 and 37% of OC (Figures 2 and S5). It was noticed that for biomass burning OC and OC_{sec}, their
258 inter-campaign differences showed comparable absolute values but opposite signs. This explains
259 why the two heating seasons had significantly different OC sources but almost the same OC levels.

260 As shown in Figure 3, OC_{sec} exhibited a positive dependence on RH, with an explosive increase

of OC_{sec} after RH exceeded 80%. Only ~6% of the 2018–2019 samples (10 out of 180) experienced such humid conditions, whereas this fraction was as high as ~37% for 2019–2020 (corresponding to 42 out of the 112 samples). Thus the potential influence of RH on SOA formation was primarily investigated based on results from the 2019–2020 campaign. Figure 4 compares OC source apportionment results across different RH ranges (< 60%, 60–80% and > 80%), which are termed low-, medium- and high-RH conditions, respectively, for this measurement period. Not only OC_{sec} but also its contribution to OC (f_{sec}) increased significantly from the low- through high-RH conditions, by factors of 9.8 and 2.6, respectively. Although the 2019–2020 campaign experienced much lower ambient temperatures (as low as –20 °C) compared to Beijing's winter (~0 °C), the f_{sec} of Harbin reached 42% for the RH range of > 80%, generally comparable with the typical range of oxygenated organic aerosol (OOA) contribution (~35–60%) determined under humid winter conditions in Beijing (Sun et al., 2013, 2014, 2018; Hu et al., 2016; Xu et al., 2019). Given the considerable AWC levels predicted for the high-RH conditions (typically above 50 μg/m^3; Figure 3), it was inferred that heterogeneous reactions might be at play in the RH-dependent increase of f_{sec}.

The OC to EC ratio (OC/EC) is also a commonly used indicator for SOA, giving rise to the EC-tracer method for the estimation of OC_{sec} mass. However, it has long been recognized that SOA formation is usually not the only factor that can increase OC/EC, and another factor that could be playing a crucial role is the biomass smoke with relatively high emission ratios of OC to EC. Among the three primary factors resolved in this study, OC/EC for the primary emissions of BB-1 (extremely high as negligible EC was apportioned to this factor; Figure S4) and BB-2 (3.5) were both larger than that of non-BB_{pri} (2.8). Thus the influences of not only SOA but also biomass

283 burning emissions need to be considered when interpreting the observed OC/EC. For the 2018–2019
284 campaign, the temporal variation of OC/EC was mainly driven by biomass burning emissions
285 (especially the BB-1 factor), as can be seen from the positive dependence of OC/EC on levoglucosan
286 and the comparison of OC/EC across the three cases with increasing LG/OC (Figure S7). In this
287 case, the EC-tracer method should be used with caution, since the basic assumption, i.e., variation
288 of OC/EC can be attributed primarily to SOA formation, was invalid. Unlike 2018–2019, SOA was
289 the dominant driver for the variation of OC/EC during the 2019–2020 measurement period, as
290 indicated by the positive dependence of OC/EC on sulfate and the comparison of OC/EC across the
291 low- through high-RH conditions (Figure S8). During the 2019–2020 campaign, similar patterns of
292 temporal variation were observed for OC_{sec} retrieved using the EC-tracer method and PMF approach,
293 and both results supported the RH-dependent increase of OC_{sec} (Figure S9). However, compared to
294 the PMF-based f_{sec}, the EC-tracer method resulted in a higher contribution of OC_{sec} to OC for the
295 high-RH conditions (60% vs. 42%). This is not surprising, as variation of biomass burning emissions
296 could also contribute to the elevated OC/EC of the high-RH conditions (Figure S8), but this
297 contribution could not be distinguished from that of SOA by the EC-tracer method. Nonetheless,
298 enhanced SOA formation was evident for the high-RH conditions, which mainly occurred within
299 the coldest months (December and January) during the 2019–2020 measurement period.

300 **3.3 Variation of secondary inorganic aerosol**

301 Both sulfate and SOR exhibited increasing trends as RH became higher (Figure 5), e.g., SOR
302 averaged 0.09 ± 0.04 and 0.20 ± 0.07 for the RH ranges of below and above 80%, respectively. The
303 apparent increase of SOR after RH exceeded 80% pointed to enhanced sulfate formation,
304 presumably through heterogeneous reactions given the high AWC levels (as can be seen from Figure

3). In addition, NO_2 appeared to be at play in the heterogeneous conversion of SO_2 to sulfate, because the RH-dependent increase of SOR was more significant for the samples with relatively high NO_2 concentrations (e.g., above 30 μg/m^3; Figure 6). Based on the observational results available, however, it was inconclusive whether NO_2 was the dominant oxidant for the heterogeneous formation of sulfate. Simulation results by ISORROPIA-II suggested moderately acidic aerosols (pH of 4.2 ± 1.1) for the high-RH conditions, and the importance of other oxidants (e.g., H_2O_2) could be comparable with or even overwhelm NO_2 for the oxidation of SO_2 in aerosol water at such pH levels (Guo et al., 2017b; Liu et al., 2017; Ye et al., 2018; Wang et al., 2021b). Nonetheless, the relationship between SOR and RH observed in Harbin was in general consistent with the wintertime results from Beijing. However, the threshold RH for sharp increase of SOR was higher in Harbin (80%) than that in Beijing (~40–70%), and the SOR in Harbin with RH above 80% (averaging 0.2) were at the lower end of the corresponding values observed during winter in Beijing (typically with averages of ~0.2–0.6) (Sun et al., 2013; Zheng et al., 2015b; Zhang et al., 2018; Li et al., 2019a; Liu et al., 2020b). A likely cause for these differences was the relatively low temperatures during the measurement period, which would reduce the rate coefficients of relevant aqueous-phase reactions (Cheng et al., 2016).

The 2018–2019 and 2019–2020 campaigns exhibited comparable sulfate concentrations for the RH range of below 80%, with median values of 3.72 and 3.39 μg/m^3, respectively (Figure S10). RH-dependent increase of sulfate was evident for both campaigns but was less significant for the former one, e.g., the median sulfate were 5.32 and 15.84 μg/m^3 for the high-RH conditions of 2018–2019 and 2019–2020, respectively. As mentioned earlier, only 10 out of the 180 samples from the 2018–2019 campaign fell into the high-RH conditions. Among these 10 samples, the RH-dependent

increase of sulfate was observed for only three ones with NO_2 concentrations of above 60 μg/m^3, but was not evident for the remaining samples which had much lower NO_2 (mostly below 30 μg/m^3; Figure 7). For the 2019–2020 campaign, however, the majority of the samples with RH above 80% showed NO_2 concentrations of above 60 μg/m^3, accompanied with elevated sulfate. Therefore, the different NO_2 levels under high-RH conditions between the two campaigns (with median concentrations of 21.27 and 72.41 μg/m^3 during 2018–2019 and 2019–2020, respectively; Figure S11) was a likely cause of the more significant RH-dependent increase of sulfate observed during the 2019–2020 campaign.

The 2019–2020 campaign also exhibited more significant RH-dependent increase of nitrate, similar to sulfate (Figure S12). In addition, an obvious difference between the two campaigns was that the nitrate to sulfate (NO_3^-/SO_4^{2-}) ratios tended to be higher during 2019–2020 (Figure S13), with an average of 1.28 ± 0.51 (compared to 1.10 ± 0.66 for 2018–2019). This trend was somewhat surprising, as the 2019–2020 measurement period experienced substantially lower temperatures than 2018–2019 (Figure S13) and consequently was expected to be impacted by stronger heating-induced coal combustion emissions, which were a large source of SO_2. However, SO_2 were actually lower for the 2019–2020 campaign, presumably due to the implementation of clean air actions targeting pollutants from coal combustion. On the other hand, NO_2 were higher during 2019–2020. Factors responsible for this increase were unclear, while a possible explanation was that the meteorological conditions of 2019–2020 were generally less favorable for dispersion of air pollutions, as indicated by the frequent occurrences of high RH. In this case, the decrease of SO_2 emissions in 2019–2020 was inferred to be more significant after accounting for the unfavorable meteorological conditions. In general, the 2019–2020 campaign exhibited higher NO_2 to SO_2 ratios

(Figure S13), which were in line with the observed variation of nitrate to sulfate ratios.

In addition to the relative abundances of NO_2 and SO_2, the influence of their gas-to-particle conversion ratios should also be considered when comparing NO_3^-/SO_4^{2-} across different conditions. The two campaigns differed with respect to humidity levels and biomass burning emissions, both of which could influence SNA formation. Although NOR and SOR were indeed influenced by RH, NO_3^-/SO_4^{2-} did not show clear dependence on RH (Figure S14). In addition, there were observational evidences indicating that biomass burning emissions could enhance photochemical oxidation of NO_2 whereas this effect was much weaker for SO_2 (Akagi et al., 2012; Collier et al., 2016), i.e., stronger BB impacts favor the increase of NO_3^-/SO_4^{2-}. Therefore, the larger NO_3^-/SO_4^{2-} during the 2019–2020 campaign could not be explained by the reduced BB influences or the elevated RH levels, and instead should be attributed primarily to the higher NO_2 to SO_2 ratios. The increasing trend of NO_2/SO_2 observed in this study was consistent with inventory results which typically indicated a more rapid decrease of SO_2 emissions compared to NO_2 during recent years in China (Zheng et al., 2018).

3.4 Variation of aerosol composition

The discussions above indicated significant differences between the two campaigns regarding the characteristics of both primary emissions and secondary aerosol formation. This in turn resulted in substantially different aerosol compositions between the two measurement periods, with the dominant drivers for the variation of aerosol composition being different as well (Figure 8).

For the 2018–2019 campaign, the contribution of OA to $(PM_{2.5})^*$ was much higher than that of SNA (60 vs. 28%). The variation of $(PM_{2.5})^*$ composition was driven mainly by biomass burning emissions (especially those from agricultural fires), which tended to increase the OA contribution

and correspondingly decrease the relative abundance of SNA. During the most intensive BB episodes (with LG/OC above 3.0%), the OA contribution reached 66% whereas the SNA contribution dropped to 23%. For the 2019–2020 campaign, however, the contribution of SNA to $(PM_{2.5})^*$ was largely comparable with OA (41 vs. 49%), and heterogeneous chemistry became the dominant driver for the variation of $(PM_{2.5})^*$ composition. The relative abundances of both SNA and SOA increased considerably from the low-RH through high-RH conditions, with their total contributions reaching 62% for the RH range of above 80%.

During the 2019–2020 measurement period, significantly higher levels of major secondary ions were observed than 2018–2019, i.e., the total concentrations of sulfate, nitrate and ammonium (SNA) averaged 27.30 and 15.53 μg/m^3, respectively. This difference was largely explained by the RH-dependence. For the 2019–2020 campaign, the sampling events with RH above 80% were mainly encountered in January of 2020 (N = 20) as well as in December of 2019 (N = 17), when the daily average temperatures were typically below –10°C. The frequent occurrences of high RH were uncommon for Harbin's winter, as can be seen from the comparison of RH in January across the past twenty years (Figure 9). Thus, the 2019–2020 campaign provided a unique opportunity to explore heterogeneous chemistry in Chinese cities located in the severe cold climate region, and might be considered as an upper limit regarding the RH-dependent enhancement of secondary aerosols. On the other hand, the effective increase of SNA and SOA under high-RH conditions implied the abundances of gaseous precursors, both organic and inorganic. To avoid the occurrence of extreme pollution events, a more fundamental solution would point to the effective control of gaseous pollutants.

3.5 Agricultural fires missed by the 2019–2020 campaign

393 The 2019–2020 campaign was designed to cover the entire heating season but was interrupted
394 by the outbreak of COVID-19. Although there was no observational result on aerosol composition
395 after 5 February, 2020, a severe $PM_{2.5}$ episode caused by agricultural fires was identified during 17–
396 18 April, 2020, as indicated by the intensive fire counts recorded for Harbin and the surrounding
397 areas (Figure 10). According to the open-access air quality data, the 24-hour $PM_{2.5}$ in Harbin reached
398 ~500 and 900 μg/m^3 on these two days, respectively, with the hourly concentrations peaking at
399 ~2350 μg/m^3. During this period, similarly high $PM_{2.5}$ levels were observed for a nearby city, Suihua,
400 which is located in the same region (the Song-Nen Plain) as Harbin. Based on a synthesis of air
401 quality data and air mass trajectory, we found that the massive amounts of air pollutants in the
402 Harbin-Suihua region, which were emitted by the agricultural fires within a concentrated period of
403 two days, could be transported ~500 km northward to Heihe, a city located on the border between
404 China and Russia. As shown in Figures 10 and S15, $PM_{2.5}$ in Heihe started to increase when the
405 back trajectory suggested air masses passing over the Harbin-Suihua region, resulting in an episode
406 with a peak $PM_{2.5}$ concentration of ~310 μg/m^3. The discussions above indicated that although
407 agricultural fires were not evident during the 2019–2020 measurement period, they were postponed
408 to late April of 2020. Thus, agricultural fires were not actually eliminated by the toughest-ever
409 policy on open burning, but broke out within a short period before the planting of crops in spring
410 instead. It is noteworthy that the intensive open burning activities resulted in not only off-the-chart
411 air pollutions for the nearby cities but also heavily-polluted episodes for downwind regions far away
412 from the source areas. We suggest that transboundary transport of agricultural fire emissions from
413 the Northeast Plain, especially the two provinces of Heilongjiang and Jilin, deserves more attention.

414 **4. Conclusions**

Significant differences were observed between aerosol properties measured during two sequential heating seasons in the central city of the HC metropolitan area, i.e., Harbin. Briefly, the differences were caused by inter-campaign variations of both primary emissions and secondary aerosol formation. The 2018–2019 measurement period was characterized by (i) frequent occurrences of agricultural fires, which were boosted by the "legitimate burning" policy, and (ii) overall low RH levels which were unfavorable for heterogeneous formation of secondary aerosols. Correspondingly, the observed $(PM_{2.5})^*$ was dominated by organic aerosol, with a substantially higher contribution than SNA (60 vs. 28%). Biomass burning emissions were the largest OC source for this measurement period. The BB to OC contribution (f_{BB}) was 46% before the onset of "legitimate burning" primarily due to household burning of crop residues, and increased to 59% after the onset of "legitimate burning" with the major contribution from agricultural fire emissions. In addition to OC, the temporal variations of $(PM_{2.5})^*$ mass concentration and chemical composition were mainly driven by biomass burning as well, especially by agricultural fires. The average $(PM_{2.5})^*$ reached ~100 μg/m^3 for the most intensive BB episodes, with an enhanced OA contribution of 66% and a reduced SNA contribution of 23%.

Compared to 2018–2019, the 2019–2020 campaign was influenced by (i) a transition of open burning policy, i.e., agricultural fires were strictly prohibited, and (ii) frequent occurrences of high-RH conditions. In this case, no evidence was observed to indicate apparent influence of agricultural fires, and correspondingly, the f_{BB} (39%) was dominated by household burning of crop residues. In addition, both SNA and secondary OC (OC_{sec}) exhibited significant RH-dependent increases. For the RH range of above 80%, SOR and the OC_{sec} to OC contribution reached 0.2 and 42%, respectively, despite the low ambient temperatures encountered (averaging about –16°C in terms of

437 daily average). Unlike 2018–2019, organic aerosol and SNA showed comparable contributions to
438 $(PM_{2.5})^*$ for the 2019–2020 campaign (49 vs. 41%), and the variations of $(PM_{2.5})^*$ during this
439 measurement period were mainly driven by secondary components.

440 **5. Implications**

441 This study has crucial implications for further improving the air quality in HC region. First, f_{BB}
442 remained relatively high for the heating season of Harbin (e.g., compared to the wintertime results
443 from Beijing), even without apparent influence of agricultural fires. This highlights the importance
444 of reducing domestic use of crop residues, on top of previous clean air actions implemented for the
445 residential sector primarily focusing on coal combustion. Second, driven by the transition of open
446 burning policy, agricultural fires exhibited different patterns but were never eliminated. For example,
447 although there was no "legitimate burning" period during 2019–2020 and agricultural fires did not
448 occur as frequently as during 2018–2019, burning did break out in spring of 2020 before crop
449 planting. Thus, neither the "legitimate burning" policy released in 2018 nor the toughest-ever "strict
450 prohibition" policy released in 2019 could be considered successful for the effective control of
451 agricultural fires. More studies are necessary to design a new roadmap towards sustainable use of
452 crop residues in Northeast China, which may contribute to the dual targets of air quality
453 improvement and climate change mitigation. Third, it is noteworthy that $(PM_{2.5})^*$ averaged ~115
454 $\mu g/m^3$ for the high-RH conditions of 2019–2020, even higher than results from the most intensive
455 BB episodes during 2018–2019. This reveals the need for effective control of gaseous precursors,
456 both organic and inorganic, of secondary aerosols. Given the increasing trends of NO_2/SO_2 and
457 NO_3^-/SO_4^{2-} observed between 2018 and 2020, control of the NO_2-related sources should be
458 strengthened.

459 It should be noted that the discussions on heterogeneous formation of SOA and SNA did not
460 necessarily exclude the reactions in fog/cloud water. Actually, based on the observational results
461 available, we could not robustly distinguish the relative importance of various aqueous-phases
462 pathways for secondary aerosol formation. To address this problem, air quality modeling with a
463 focus on HC should be conducted in future studies, which could also quantitatively evaluate the
464 contributions of various factors (e.g., meteorology, emissions and regional transport) to long-term
465 trends of $PM_{2.5}$ concentration and chemical composition. An essential precondition is that the model
466 could properly re-produce the observational results, which appears a substantial challenge for
467 Harbin as indicated by the limited inter-comparison studies, especially for the periods with intensive
468 agricultural fires or high RH levels (Cheng et al., 2021b).

469 **Data availability.**

470 Data are available from the corresponding author upon request (jiumengliu@hit.edu.cn).

471 **Author contribution**

472 YC and JL designed the study and prepared the paper with inputs from all the coauthors. QY, XC,
473 YZ, ZD and LL carried out the experiments. GG provided the air quality data. WM and HQ
474 participated in the field campaign and data analysis. QZ and KB supervised the study.

475 **Competing interests.**

476 The authors declare that they have no conflict of interest.

477 **Acknowledgements**

478 This work was supported by the National Natural Science Foundation of China (41805097), the
479 Natural Science Foundation of Heilongjiang Province (YQ2019D004), the State Key Laboratory of
480 Urban Water Resource and Environment (2020DX14), the State Key Joint Laboratory of

Environment Simulation and Pollution Control (19K02ESPCT), the State Environmental Protection Key Laboratory of Sources and Control of Air Pollution Complex (SCAPC202002) and Heilongjiang Touyan Team.

References

Akagi, S. K., Craven, J. S., Taylor, J. W., McMeeking, G. R., Yokelson, R. J., Burling, I. R., Urbanski, S. P., Wold, C. E., Seinfeld, J. H., Coe, H., Alvarado, M. J., and Weise, D. R.: Evolution of trace gases and particles emitted by a chaparral fire in California, ***Atmos. Chem. Phys.***, 12, 1397–1421, 2012.

Cao, F., Zhang, S. C., Kawamura, K., and Zhang, Y. L.: Inorganic markers, carbonaceous components and stable carbon isotope from biomass burning aerosols in Northeast China, ***Sci. Total Environ.***, 572, 1244–1251, 2016.

Cheng, Y., Yu, Q. Q., Liu, J. M., Du, Z. Y., Liang, L. L., Geng, G. N., Zheng, B., Ma, W. L., Qi, H., Zhang, Q., and He, K.B.: Strong biomass burning contribution to ambient aerosol during heating season in a megacity in Northeast China: effectiveness of agricultural fire bans?, ***Sci. Total Environ.***, 754, 142144, 2021a.

Cheng, Y., Yu, Q. Q., Liu, J. M., Zhu, S. Q., Zhang, M. Y., Zhang, H. L., Zheng, B., and He, K. B.: Model vs. observation discrepancy in aerosol characteristics during a half-year long campaign in Northeast China: the role of biomass burning, ***Environ. Pollut.***, 269, 116167, 2021b.

Cheng, Y. F., Zheng, G. J., Wei, C., Mu, Q., Zheng, B., Wang, Z. B., Gao, M., Zhang, Q., He, K. B., Carmichael, G., Pöschl, U., and Su, H.: Reactive nitrogen chemistry in aerosol water as a source of sulfate during haze events in China, ***Sci. Adv.***, 2, e1601530, 2016.

Collier, S., Zhou, S., Onasch, T. B., Jaffe, D. A., Kleinman, L., Sedlacek, A. J., Briggs, N. L., Hee, J., Fortner, E., Shilling, J. E., Worsnop, D., Yokelson, R. J., Parworth, C., Ge, X. L., Xu, J. Z., Butterfield, Z., Chand, D., Dubey, M. K., Pekour, M. S., Springston, S., and Zhang, Q.: Regional influence of aerosol emissions from wildfires driven by combustion efficiency: insights from the BBOP campaign, ***Environ. Sci. Technol.***, 50, 8613–8622, 2016.

Department of Ecology and Environment of Heilongjiang Province: Interim Provisions of Heilongjiang Province on Reward and Punishment for Straw Open Burning Management,

509 available at: http://www.gov.cn/xinwen/2018-09/15/content_5322298.htm (last access: June
510 17, 2021), 2018.
511 Fountoukis, C., and Nenes, A.: ISORROPIA II: a computationally efficient thermodynamic
512 equilibrium model for K^+–Ca^{2+}–Mg^{2+}–NH_4^+–Na^+–SO_4^{2-}–NO_3^-–Cl^-–H_2O aerosols, ***Atmos. Chem. Phys.***, 7, 4639–4659, 2007.
513
514 Guo, H. Y., Liu, J. M., Froyd, K. D., Roberts, J. M., Veres, P. R., Hayes, P. L., Jimenez, J. L., Nenes,
515 A., and Weber, R. J.: Fine particle pH and gas–particle phase partitioning of inorganic species
516 in Pasadena, California, during the 2010 CalNex campaign, ***Atmos. Chem. Phys.***, 17, 5703–
517 5719, 2017a.
518 Guo, H. Y., Weber, R. J., and Nenes, A.: High levels of ammonia do not raise fine particle pH
519 sufficiently to yield nitrogen oxide-dominated sulfate production, ***Sci. Rep.***, 7, 12109, 2017b.
520 Hu, W. W., Hu, M., Hu, W., Jimenez, J. L., Yuan, B., Chen, W. T., Wang, M., Wu, Y. S., Chen, C.,
521 Wang, Z. B., Peng, J. F., Zeng, L. M., and Shao, M.: Chemical composition, sources, and aging
522 process of submicron aerosols in Beijing: contrast between summer and winter, ***J. Geophys. Res. Atmos.***, 121, 1955–1977, 2016.
523
524 Huang, X., Ding, A. J., Gao, J., Zheng, B., Zhou, D. R., Qi, X. M., Tang, R., Wang, J. P., Ren, C.
525 H., Nie, W., Chi, X. G., Xu, Z., Chen, L. D., Li, Y. Y., Che, F., Pang, N., Wang, H. K., Tong,
526 D., Qin, W., Cheng, W., Liu, W. J., Fu, Q. Y., Liu, B. X., Chai, F. H., Davis, S. J., Zhang, Q.,
527 and He, K. B.: Enhanced secondary pollution offset reduction of primary emissions during
528 COVID-19 lockdown in China, ***Natl. Sci. Rev.***, 8, nwaa137, 2021.
529 Kuang, Y., He, Y., Xu, W. Y., Yuan, B., Zhang, G., Ma, Z. Q., Wu, C. H., Wang, C. M., Wang, S. H.,
530 Zhang, S. Y., Tao, J. C., Ma, N., Su, H., Cheng, Y. F., Shao, M., and Sun, Y. L.: Photochemical
531 aqueous-phase reactions induce rapid daytime formation of oxygenated organic aerosol on the
532 North China Plain, ***Environ. Sci. Technol.***, 54, 3849–3860, 2020.
533 Le, T. H., Wang, Y., Liu, L., Yang, J. N., Yung, Y. L., Li, G. H., and Seinfeld, J. H.: Unexpected air
534 pollution with marked emission reductions during the COVID-19 outbreak in China, ***Science***,
535 369, 702–706, 2020.
536 Li, H. Y., Cheng, J., Zhang, Q., Zheng, B., Zhang, Y. X., Zheng, G. J., and He, K. B.: Rapid transition
537 in winter aerosol composition in Beijing from 2014 to 2017: response to clean air actions,
538 ***Atmos. Chem. Phys.***, 19, 11485–11499, 2019a.

Li, Y. C., Liu, J., Han, H., Zhao, T. L., Zhang, X., Zhuang, B. L., Wang, T. J., Chen, H. M., Wu, Y., and Li, M. M.: Collective impacts of biomass burning and synoptic weather on surface $PM_{2.5}$ and CO in Northeast China, ***Atmos. Environ.***, 213, 64–80, 2019b.

Liu, J. M., Wang, P. F., Zhang, H. L., Du, Z. Y., Zheng, B., Yu, Q. Q., Zheng, G. J., Ma, Y. L., Zheng, M., Cheng, Y., Zhang, Q., and He, K. B.: Integration of field observation and air quality modeling to characterize Beijing aerosol in different seasons, ***Chemosphere***, 242, 125195, 2020a.

Liu, J. M., Alexander, L., Fast, J. D., Lindenmaier, R., Shilling, J. E.: Aerosol characteristics at the Southern Great Plains site during the HI-SCALE campaign, ***Atmos. Chem. Phys.***, 21, 5101–5116, 2021a.

Liu, P. F., Ye, C., Xue, C. Y., Zhang, C. L., Mu, Y. J., and Sun, X.: Formation mechanisms of atmospheric nitrate and sulfate during the winter haze pollution periods in Beijing: gas-phase, heterogeneous and aqueous-phase chemistry, ***Atmos. Chem. Phys.***, 20, 4153–4165, 2020b.

Liu, T. Y., Chan, A. W. H., and Abbatt, J. P. D.: Multiphase oxidation of sulfur dioxide in aerosol particles: implications for sulfate formation in polluted environments, ***Environ. Sci. Technol.***, 8, 4227–4242, 2021b.

Lv, Z. F., Wang, X. T., Deng, F. Y., Ying, Q., Archibald, A. T., Jones, R. L., Ding, Y., Cheng, Y., Fu, M. L., Liu, Y., Man, H. Y., Xue, Z. G., He, K. B., Hao, J. M., and Liu, H.: Source-receptor relationship revealed by the halted traffic and aggravated haze in Beijing during the COVID-19 lockdown, ***Environ. Sci. Technol.***, 54, 15660–15670, 2020.

May, A. A., McMeeking, G. R., Lee, T., Taylor, J. W., Craven, J. S., Burling, I., Sullivan, A. P., Akagi, S., Collett, J. L., Flynn, M., Coe, H., Urbanski, S. P., Seinfeld, J. H., Yokelson, R. J., and Kreidenweis, S. M.: Aerosol emissions from prescribed fires in the United States: a synthesis of laboratory and aircraft measurements, ***J. Geophys. Res. Atmos.***, 119, 11826–11849, 2014.

McClure, C. D., Lim, C. Y., Hagan, D. H., Kroll, J. H., Cappa, C. D.: Biomass-burning-derived particles from a wide variety of fuels – Part 1: properties of primary particles, ***Atmos. Chem. Phys.***, 20, 1531–1547, 2020.

McMeeking, G. R., Kreidenweis, S. M., Baker, S., Carrico, C. M., Chow, J. C., Collett, J. L., Hao, W. M., Holden, A. S., Kirchstetter, T. W., Malm, W. C., Moosmüller, H., Sullivan, A. P., and

569 Wold, C. E.: Emissions of trace gases and aerosols during the open combustion of biomass in
570 the laboratory, ***J. Geophys. Res.***, 114, D19210, 2009.
571 National Bureau of Statistics of China: China Statistical Yearbook 2020, available at:
572 http://www.stats.gov.cn/tjsj/ndsj/2020/indexeh.htm, 2020.
573 Pokhrel, R. P., Wagner, N. L., Langridge, J. M., Lack, D. A., Jayarathne, T., Stone, E. A., Stockwell,
574 C. E., Yokelson, R. J., and Murphy, S. M.: Parameterization of single-scattering albedo (SSA)
575 and absorption Ångström exponent (AAE) with EC/OC for aerosol emissions from biomass
576 burning, ***Atmos. Chem. Phys.***, 16, 9549–9561, 2016.
577 Shi, Z. B., Vu, T., Kotthaus, S., Harrison, R. M., Grimmond, S., Yue, S. Y., Zhu, T., Lee, J., Han, Y.
578 Q., Demuzere, M., Dunmore, R. E., Ren, L. J., Liu, D., Wang, Y. L., Wild, O., Allan, J., Acton,
579 W. J., Barlow, J., Barratt, B., Beddows, D., Bloss, W. J., Calzolai, G., Carruthers, D., Carslaw,
580 D. C., Chan, Q., Chatzidiakou, L., Chen, Y., Crilley, L., Coe, H., Dai, T., Doherty, R., Duan, F.
581 K., Fu, P. Q., Ge, B. Z., Ge, M. F., Guan, D. B., Hamilton, J. F., He, K. B., Heal, M., Heard, D.,
582 Hewitt, C. N., Hollaway, M., Hu, M., Ji, D. S., Jiang, X. J., Jones, R., Kalberer, M., Kelly, F.
583 J., Kramer, L., Langford, B., Lin, C., Lewis, A. C., Li, J., Li, W. J., Liu, H., Liu, J. F., Loh, M.,
584 Lu, K. D., Lucarelli, F., Mann, G., McFiggans, G., Miller, M. R., Mills, G., Monk, P., Nemitz,
585 E., O'Connor, F., Ouyang, B., Palmer, P. I., Percival, C., Popoola, O., Reeves, C., Rickard, A.
586 R., Shao, L. Y., Shi, G. Y., Spracklen, D., Stevenson, D., Sun, Y. L., Sun, Z. W., Tao, S., Tong,
587 S. R., Wang, Q. Q., Wang, W. H., Wang, X. M., Wang, X. J., Wang, Z. F., Wei, L. F., Whalley,
588 L., Wu, X. F., Wu, Z. J., Xie, P. H., Yang, F. M., Zhang, Q., Zhang, Y. L., Zhang, Y. H., and
589 Zheng, M.: Introduction to the special issue “In-depth study of air pollution sources and
590 processes within Beijing and its surrounding region (APHH-Beijing)”, ***Atmos. Chem. Phys.***,
591 19, 7519–7546, 2019.
592 Shrivastava, M., Cappa, C. D., Fan, J. W., Goldstein, A. H., Guenther, A. B., Jimenez, J. L., Kuang,
593 C., Laskin, A., Martin, S. T., Ng, N. L., Petaja, T., Pierce, J. R., Rasch, P. J., Roldin, P., Seinfeld,
594 J. H., Shilling, J., Smith, J. N., Thornton, J. A., Volkamer, R., Wang, J., Worsnop, D. R., Zaveri,
595 R. A., Zelenyuk, A., and Zhang, Q.: Recent advances in understanding secondary organic
596 aerosol: implications for global climate forcing, ***Rev. Geophys.***, 55, 509–559, 2017.
597 Song, S. J., Gao, M., Xu, W. Q., Shao, J. Y., Shi, G. L., Wang, S. X., Wang, Y. X., Sun, Y. L., and
598 McElroy, M. B.: Fine-particle pH for Beijing winter haze as inferred from different

599 thermodynamic equilibrium models, ***Atmos. Chem. Phys.***, 18, 7423–7438, 2018.
600 Su, H., Cheng, Y. F., and Pöschl, U.: New multiphase chemical processes influencing atmospheric
601 aerosols, air quality, and climate in the Anthropocene, ***Acc. Chem. Res.***, 53, 2034–2043, 2020.
602 Sun, Y. L., Jiang, Q., Wang, Z. F., Fu, P. Q., Li, J., Yang, T., and Yin, Y.: Investigation of the sources
603 and evolution processes of severe haze pollution in Beijing in January 2013, ***J. Geophys. Res.***
604 ***Atmos.***, 119, 4380–4398, 2014.
605 Sun, Y. L., Wang, Z. F., Fu, P. Q., Jiang, Q., Yang, T., Li, J., and Ge, X. L.: The impact of relative
606 humidity on aerosol composition and evolution processes during wintertime in Beijing, China,
607 ***Atmos. Environ.***, 77, 927–934, 2013.
608 Sun, Y. L., Xu, W. Q., Zhang, Q., Jiang, Q., Canonaco, F., Prévôt, A. S. H., Fu, P. Q., Li, J., Jayne,
609 J., Worsnop, D. R., and Wang, Z. F.: Source apportionment of organic aerosol from 2-year
610 highly time-resolved measurements by an aerosol chemical speciation monitor in Beijing,
611 China, ***Atmos. Chem. Phys.***, 18, 8469–8489, 2018.
612 Wang, G. H., Zhang, R. Y., Gomez, M. E., Yang, L. X., Zamora, M. L., Hu, M., Lin, Y., Peng, J. F.,
613 Guo, S., Meng, J. J., Li, J. J., Cheng, C. L., Hu, T. F., Ren, Y. Q., Wang, Y. S., Gao, J., Cao, J.
614 J., An, Z. S., Zhou, W. J., Li, G. H., Wang, J. Y., Tian, P. F., Marrero-Ortiz, W., Secrest, J., Du,
615 Z. F., Zheng, J., Shang, D. J., Zeng, L. M., Shao, M., Wang, W. G., Huang, Y., Wang, Y., Zhu,
616 Y. J., Li, Y. X., Hu, J. X., Pan, B. W., Cai, L., Cheng, Y. T., Ji, Y. M., Zhang, F., Rosenfeld, D.,
617 Liss, P. S., Duce, R. A., Kolb, C. E., and Molina, M. J.: Persistent sulfate formation from
618 London Fog to Chinese haze, ***Proc. Natl. Acad. Sci. U.S.A.***, 113, 13630–13635, 2016.
619 Wang, J. F., Li, J. Y., Ye, J. H., Zhao, J., Wu, Y. Z., Hu, J. L., Liu, D. T., Nie, D. Y., Shen, F. Z.,
620 Huang, X. P., Huang, D. D., Ji, D. S., Sun, X., Xu, W. Q., Guo, J. P., Song, S. J., Qin, Y. M.,
621 Liu, P. F., Turner, J. R., Lee, H. C., Hwang, S., Liao, H., Martin, S. T., Zhang, Q., Chen, M. D.,
622 Sun, Y. L., Ge, X. L., and Jacob, D. J.: Fast sulfate formation from oxidation of SO_2 by NO_2
623 and HONO observed in Beijing haze, ***Nat. Commun.***, 11, 2844, 2020a.
624 Wang, J. F., Ye, J. H., Zhang, Q., Zhao, J., Wu, Y. Z., Li, J. Y., Liu, D. T., Li, W. J., Zhang, Y. G.,
625 Wu, C., Xie, C. H., Qin, Y. M., Lei, Y. L., Huang, X. P., Guo, J. P., Liu, P. F., Fu, P. Q., Li, Y.
626 J., Lee, H. C., Choi, H., Zhang, J., Liao, H., Chen, M. D., Sun, Y. L., Ge, X. L., Martin, S. T.,
627 and Jacob, D. J.: Aqueous production of secondary organic aerosol from fossil-fuel emissions
628 in winter Beijing haze, ***Proc. Natl. Acad. Sci. U. S. A.***, 118, e2022179118, 2021a.

Wang, P. F., Chen, K. Y., Zhu, S. Q., Wang, P., and Zhang, H. L.: Severe air pollution events not avoided by reduced anthropogenic activities during COVID-19 outbreak, ***Resour. Conserv. Recy.***, 158, 104814, 2020b.

Wang, W. G., Liu, M. Y., Wang, T. T., Song, Y., Zhou, L., Cao, J. J., Hu, J. N., Tang, G. G., Chen, Z., Li, Z. J., Xu, Z. Y., Peng, C., Lian, C. F., Chen, Y., Pan, Y. P., Zhang, Y. H., Sun, Y. L., Li, W. J., Zhu, T., Tian, H. Z., and Ge, M. F.: Sulfate formation is dominated by manganese-catalyzed oxidation of SO_2 on aerosol surfaces during haze events, ***Nat. Commun.***, 12, 1993, 2021b.

Wang, Y. J., Hu, M., Xu, N., Qin, Y. H., Wu, Z. J., Zeng, L. W., Huang, X. F., and He, L. Y.: Chemical composition and light absorption of carbonaceous aerosols emitted from crop residue burning: influence of combustion efficiency, ***Atmos. Chem. Phys.***, 20, 13721–13734, 2020c.

Wang, Y. X., Zhang, Q. Q., Jiang, J. K., Zhou, W., Wang, B. Y., He, K. B., Duan, F. K., Zhang, Q., Philip, S., and Xie, Y. Y.: Enhanced sulfate formation during China's severe winter haze episode in January 2013 missing from current models, ***J. Geophys. Res. Atmos.***, 119, 10425–10440, 2014.

Xu, W. Q., Sun, Y. L., Wang, Q. Q., Zhao, J., Wang, J. F., Ge, X. L., Xie, C. H., Zhou, W., Du, W., Li, J., Fu, P. Q., Wang, Z. F., Worsnop, D. R., and Coe, H.: Changes in aerosol chemistry from 2014 to 2016 in winter in Beijing: insights from high-resolution aerosol mass spectrometry, ***J. Geophys. Res. Atmos.***, 124, 1132–1147, 2019.

Yang, T., Gbaguidi, A., Yan, P.Z., Zhang, W.D., Zhu, L.L., Yao, X.F., Wang, Z.F., Chen, H.: Model elucidating the sources and formation mechanisms of severe haze pollution over Northeast mega-city cluster in China, ***Atmos. Environ.***, 230, 692–700, 2017.

Ye, C., Liu, P. F., Ma, Z. B., Xue, C. Y., Zhang, C. L., Zhang, Y. Y., Liu, J. F., Liu, C. T., Sun, X., and Mu, Y. J.: High H_2O_2 concentrations observed during haze periods during the winter in Beijing: importance of H_2O_2 oxidation in sulfate formation, ***Environ. Sci. Technol. Lett.***, 5, 757–763, 2018.

Zhang, J., Liu, L., Xu, L., Lin, Q. H., Zhao, H. J., Wang, Z. B., Guo, S., Hu, M., Liu, D. T., Shi, Z. B., Huang, D., and Li, W. J.: Exploring wintertime regional haze in northeast China: role of coal and biomass burning, ***Atmos. Chem. Phys.***, 20, 5355–5372, 2020.

Zhang, Q., Zheng, Y. X., Tong, D., Shao, M., Wang, S. X., Zhang, Y. H., Xu, X. D., Wang, J. N., He,

H., Liu, W. Q., Ding, Y. H., Lei, Y., Li, J. H., Wang, Z. F., Zhang, X. Y., Wang, Y. S., Cheng, J., Liu, Y., Shi, Q. R., Yan, L., Geng, G. N., Hong, C. P., Li, M., Liu, F., Zheng, B., Cao, J. J., Ding, A. J., Gao, J., Fu, Q. Y., Huo, J. T., Liu, B. X., Liu, Z. R., Yang, F. M., He, K. B., and Hao, J. M.: Drivers of improved $PM_{2.5}$ air quality in China from 2013 to 2017, ***Proc. Natl. Acad. Sci. U. S. A.***, 116, 24463–24469, 2019.

Zhang, R., Sun, X. S., Shi, A. J., Huang, Y. H., Yan, J., Nie, T., Yan, X., Li, X.: Secondary inorganic aerosols formation during haze episodes at an urban site in Beijing, China, ***Atmos. Environ.***, 177, 275–282, 2018.

Zheng, B., Tong, D., Li, M., Liu, F., Hong, C. P., Geng, G. N., Li, H. Y., Li, X., Peng, L. Q., Qi, J., Yan, L., Zhang, Y. X., Zhao, H. Y., Zheng, Y. X., He, K. B., and Zhang, Q.: Trends in China's anthropogenic emissions since 2010 as the consequence of clean air actions, ***Atmos. Chem. Phys.***, 18, 14095–14111, 2018.

Zheng, B., Zhang, Q., Zhang, Y., He, K. B., Wang, K., Zheng, G. J., Duan, F. K., Ma, Y. L., and Kimoto, T.: Heterogeneous chemistry: a mechanism missing in current models to explain secondary inorganic aerosol formation during the January 2013 haze episode in North China, ***Atmos. Chem. Phys.***, 15, 2031–2049, 2015a.

Zheng, G. J., Duan, F. K., Su, H., Ma, Y. L., Cheng, Y., Zheng, B., Zhang, Q., Huang, T., Kimoto, T., Chang, D., Pöschl, U., Cheng, Y. F., and He, K.B.: Exploring the severe winter haze in Beijing: the impact of synoptic weather, regional transport and heterogeneous reactions, ***Atmos. Chem. Phys.***, 15, 2969–2983, 2015b.

Zheng, G. J., Su, H., Wang, S. W., Andreae, M. O., Pöschl, U., and Cheng, Y. F.: Multiphase buffer theory explains contrasts in atmospheric aerosol acidity, ***Science***, 369, 1374–1377, 2020.

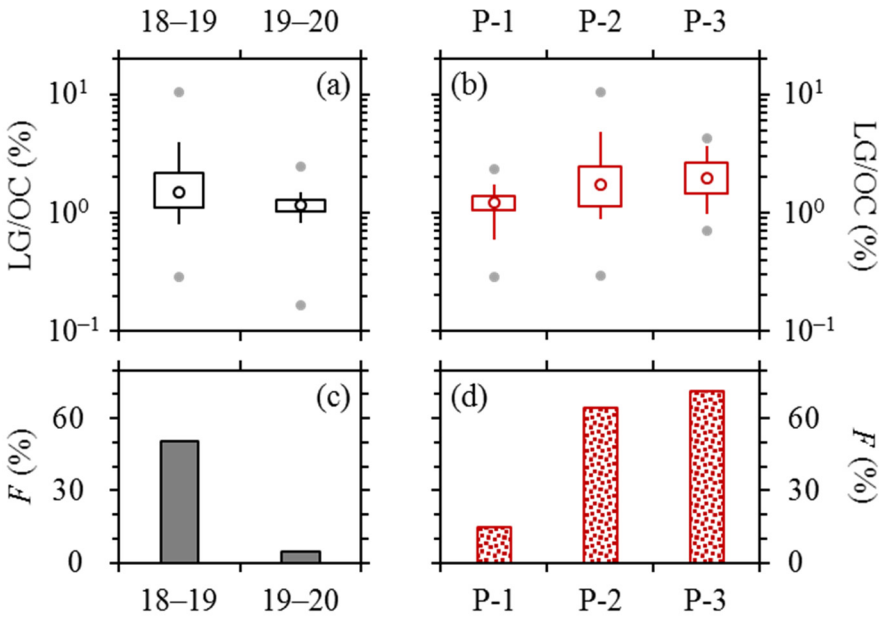

Figure 1. Comparisons of levoglucosan to OC ratios, i.e., LG/OC (on a basis of carbon mass), and the fractions of samples with LG/OC above 1.5% (denoted as *F*), **(a, c)** between the 2018–2019 and 2019–2020 campaigns, and **(b, d)** across the 2018–2019 samples collected before (P-1), during (P-2) and after (P-3) the "legitimate burning" periods. Lower and upper box bounds indicate the 25th and 75th percentiles, the whiskers below and above the box indicate the 5th and 95th percentiles, the solid circles below and above the box indicate the minimum and maximum, and the open circle within the box marks the median (the same hereinafter).

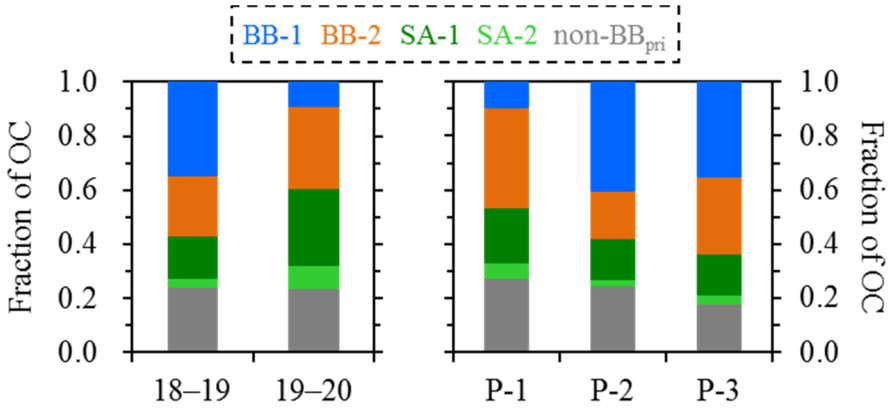

689

690 **Figure 2.** Comparison of OC source apportionment results between the 2018–2019 and 2019–2020
691 campaigns (left panel), and across the 2018–2019 samples collected before (P-1), during (P-2) and
692 after (P-3) the "legitimate burning" periods (right panel).

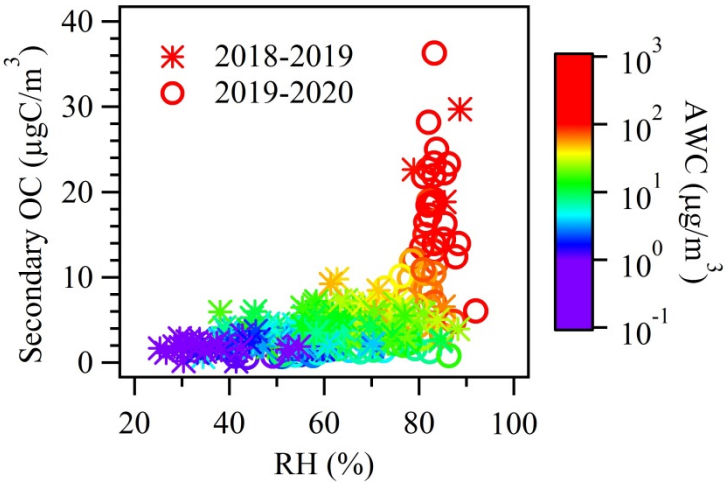

693

694 **Figure 3.** Dependence of secondary OC (OC_{sec}) on RH among the two campaigns, color-coded by
695 AWC levels. Results from the 2018–2019 campaign and 2019–2020 campaign were marked using
696 stars and circles, respectively. The majority of the data points with RH above 80% were observed
697 during 2019–2020. RH exceeded 80% for only ten samples collected during 2018–2019, and only
698 three out of these ten samples showed RH-dependent increase of OC_{sec}.

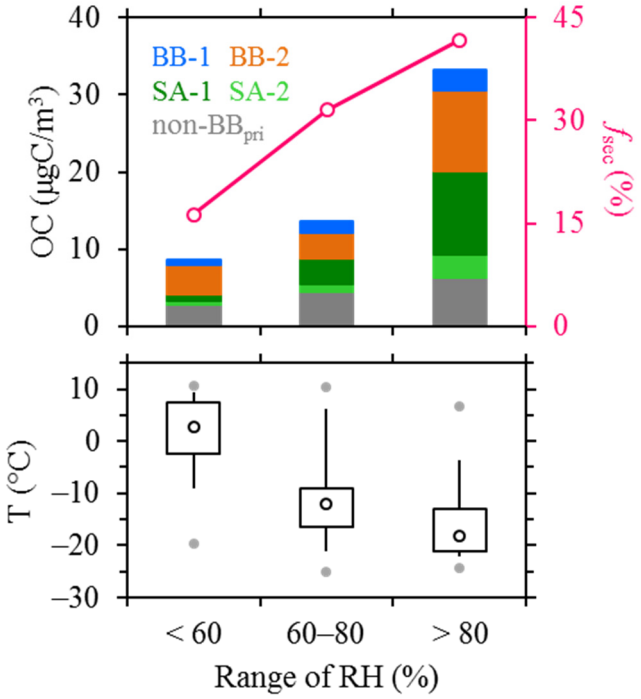

699

700 **Figure 4.** Comparisons of OC source apportionment results (upper panel, left axis), the ~~contribution~~
701 contributions of PMF-based OC_{sec} to OC (f_{sec}; upper pannel, right axis), and ambient temperatures
702 across different RH ranges (lower panel) for the 2019–2020 campaign.

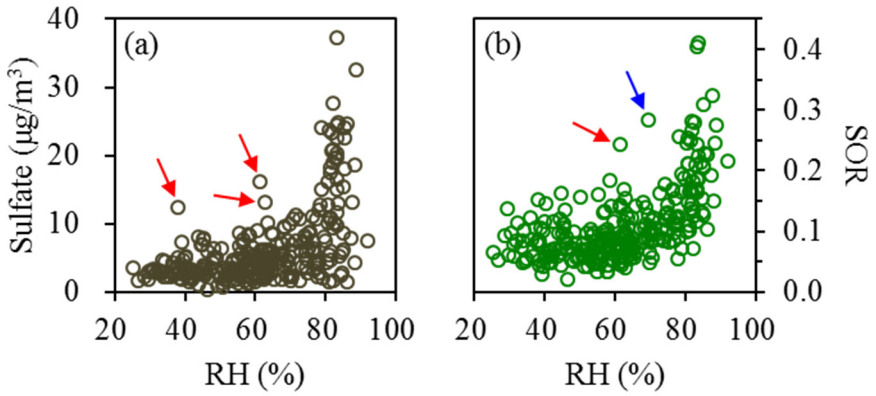

Figure 5. Dependences of **(a)** sulfate and **(b)** SOR on RH. Results from the 2018–2019 and 2019–2020 campaigns are combined. Relatively high sulfate are typically observed for the conditions with RH above 80%, which is also the case for SOR. There appear to be several outliers showing considerably higher sulfate or SOR than other samples at similar RH. All the outliers occurred during the 2018–2019 measurement period, and most of them were accompanied with extremely high levoglucosan concentrations (above 5 μg/m^3), as highlighted by the red arrows. The outlier highlighted by the blue arrow was observed ~~with~~ at an ambient temperature of above 10 °C, which was uncommon for the heating season. The outliers indicate that factors other than RH were also at play in sulfate formation, but the influences were evident for only several samples.

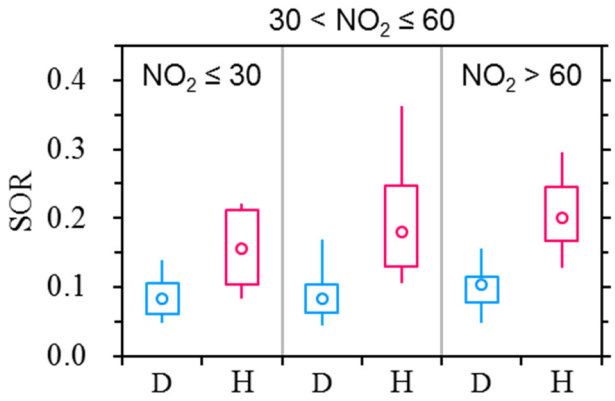

Figure 6. Comparisons of SOR between different RH levels, with results from different NO_2 ranges (below 30, 30–60 and above 60 μg/m^3) shown separately. Results from both the 2018–2019 and 2019–2020 campaigns are included. The terms "D" and "H" indicate relatively dry (RH below 80%) and more humid conditions (RH above 80%), respectively.

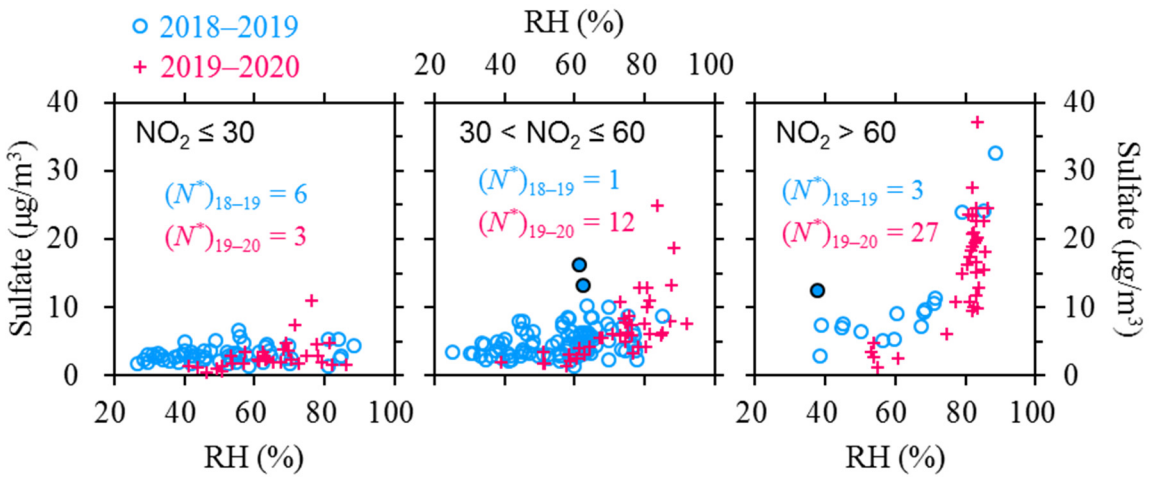

718

719 **Figure 7.** Dependences of sulfate on RH in different NO_2 ranges (below 30, 30–60 and above 60
720 μg/m^3). Results from the 2018–2019 and 2019–2020 campaigns are shown using different markers.
721 The outliers in Figure 5a are highlighted by the solid circles. N^* indicates the number of samples
722 with RH above 80%. High-RH conditions were typically accompanied with NO_2 concentrations of
723 below 30 μg/m^3 during 2018–2019, and NO_2 above 60 μg/m^3 during 2019–2020, respectively.

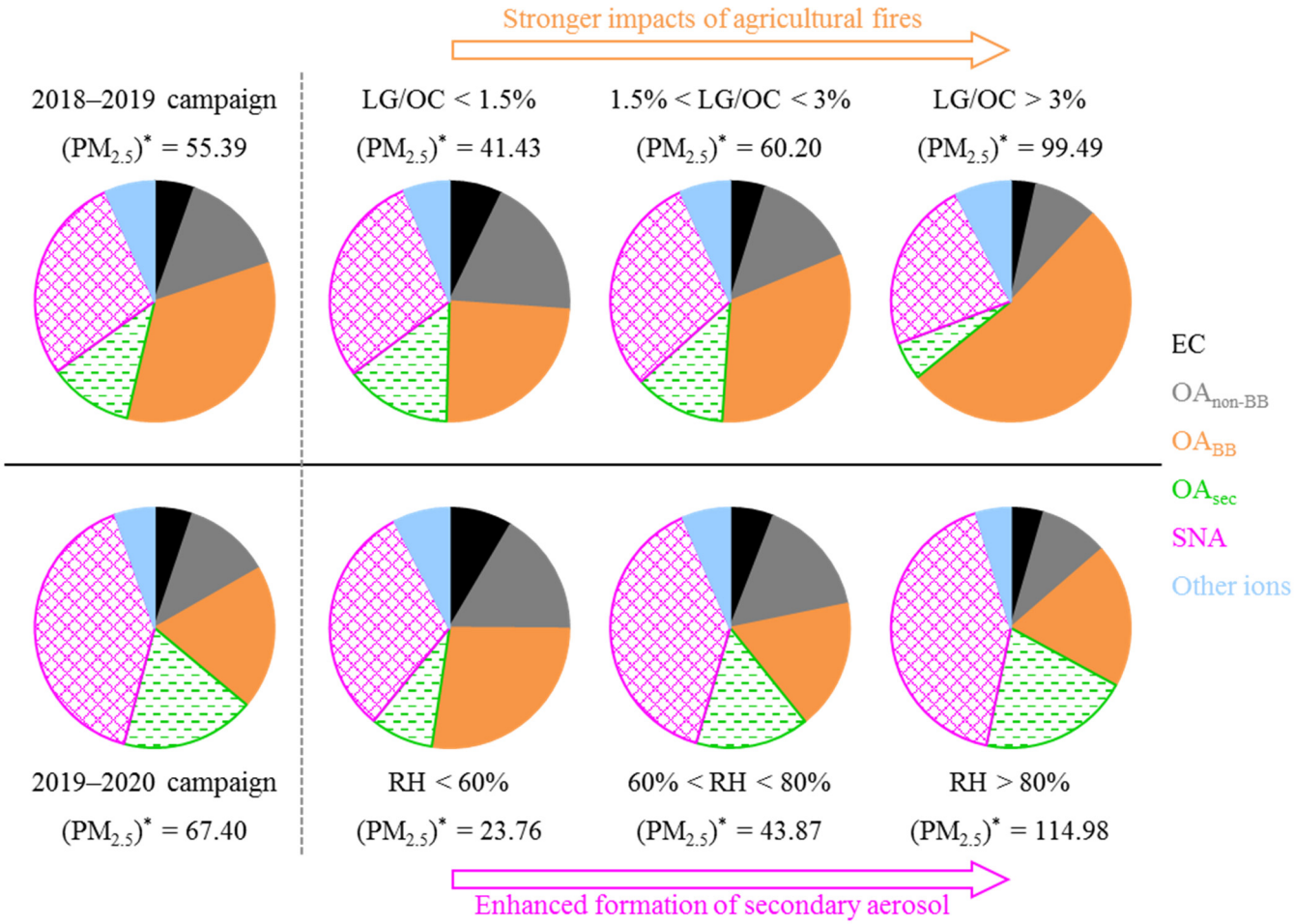

724

725 **Figure 8.** Comparison of aerosol compositions measured for the 2018–2019 and 2019–2020 campaigns. The 2018–
726 2019 measurement period experienced relatively dry meteorological conditions (with RH levels rarely exceeding
727 80%) and was characterized by a wide window of ~3 months for "legitimate burning". Correspondingly, variations
728 of $(PM_{2.5})^*$ concentration (in μg/m^3) and aerosol composition observed during 2018–2019 were mainly driven by
729 agricultural fires. However, the "legitimate burning" policy was terminated in 2019, and the 2019–2020 campaign
730 did not show clear evidence for apparent influence of agricultural fires. On the other hand, high-RH conditions
731 occurred much more frequently during the 2019–2020 measurement period compared to 2018–2019.
732 Correspondingly, variations of $(PM_{2.5})^*$ concentration and aerosol composition observed during 2019–2020 were
733 mainly driven by RH-dependent increase of secondary aerosols.

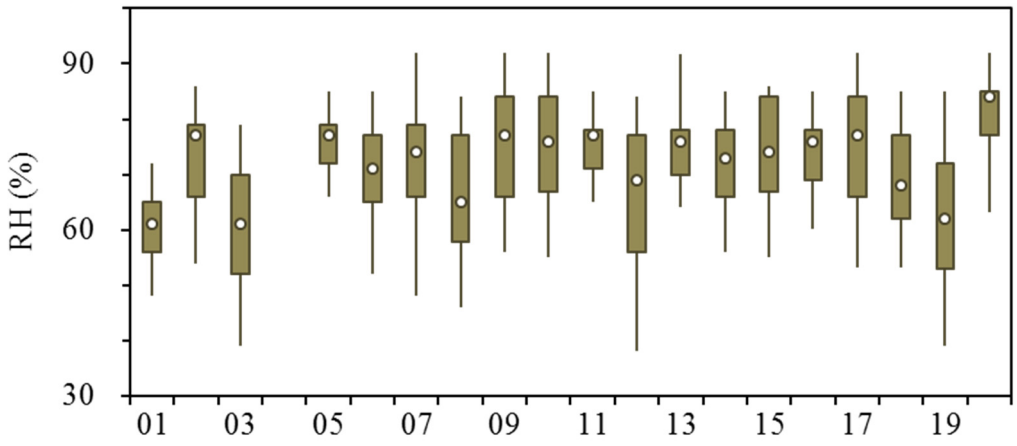

Figure 9. Comparison of RH measured during January in Harbin across the past twenty years (from 2001 through 2020). Time resolution is 1-h for the RH data. No observational result is available for January of 2004.

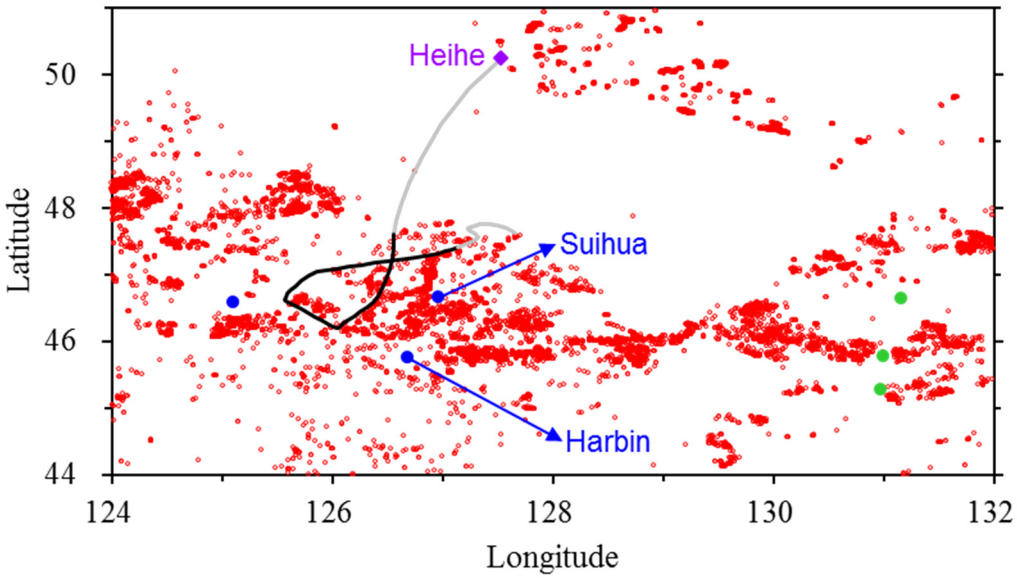

Figure 10. Active fires (red circles) detected by the joint NASA/NOAA Suomi-National Polar orbiting Partnership (S-NPP) satellite for Heilongjiang Province during 17–18 April, 2020. Three cities located in the Song-Nen Plain are shown using blue dots (the unlabeled city is Daqing), and three cities located in the San-Jiang Plain (i.e., Shuangyashan, Qitaihe and Jixi with decreasing latitudes) are shown using green dots. The two plains, separated by mountains, are the main agricultural regions in Heilongjiang. Intensive agricultural fires are evident for both plains during the two-day episode, indicating the open burning activities are province-wide, although prohibited. The agricultural fires resulted in severe $PM_{2.5}$ pollution for nearby cities, e.g., the 24-hour concentrations peaked at ~900 and 675 μg/m^3 in Harbin and Jixi, respectively. A $PM_{2.5}$ episode was observed even for Heihe (~500 km away from Harbin) on 19 April, 2020, which was attributed to the pollutants transported from the Harbin-Suihua region. The solid line indicates the 72-hour back trajectory ending at 7:00 in Heihe, accompanied with the highest 1-hour $PM_{2.5}$ observed on 19 April, 2020 (~310 μg/m^3). The trajectory indicates transport pathway of air masses impacting Heihe, with the segment in black showing locations of the air masses during 17–18 April, 2020.